

## Supporting Information

# Structural, Vibrational and Electronic Study of $\alpha$ -As<sub>2</sub>Te<sub>3</sub> under Compression

*V.P. Cuenca-Gotor,<sup>1</sup> J.A. Sans,<sup>1,\*</sup> J. Ibáñez,<sup>2</sup> C. Popescu,<sup>3</sup> O.Gomis,<sup>4</sup> R. Vilaplana,<sup>4</sup> F.J. Manjón,<sup>1</sup> A. Leonardo,<sup>5,6</sup> E. Sagasta,<sup>7</sup> A. Suárez-Alcubilla,<sup>8,9</sup> I.G. Gurtubay,<sup>6,8</sup> M. Mollar,<sup>1</sup> and A. Bergara<sup>6,8,9</sup>*

1 Instituto de Diseño para la Fabricación y Producción Automatizada, Universitat Politècnica de València, 46022 Valencia (Spain)

2 Institut de Ciències de la Terra Jaume Almera, CSIC, Barcelona (Spain)

3 ALBA-CELLS, 08290 Cerdanyola, Barcelona (Spain)

4 Centro de Tecnologías Físicas, Universitat Politècnica de València, 46022 Valencia (Spain)

5 Dpto. de Física Aplicada II, Universidad del País Vasco, UPV/EHU, 48080 Bilbao (Spain)

6 Donostia International Physics Center (DIPC), 20018 Donostia (Spain)

7 CIC NanoGUNE, E-20018, Donostia, San Sebastián (Spain)

8 Dpto. de Física de la Materia Condensada, Universidad del País Vasco, UPV/EHU, 48080 Bilbao (Spain)

9 Centro de Física de Materiales CFM, Centro Mixto CSIC-UPV/EHU, 20018 Donostia (Spain)

\*Corresponding author: J.A. Sans (juasant2@upv.es)

### Lattice dynamics of $\alpha$ -As<sub>2</sub>Te<sub>3</sub> at room pressure

The RS spectrum of  $\alpha$ -As<sub>2</sub>Te<sub>3</sub> at room pressure has a close similarity to RS spectra reported in glasses containing As and Te atoms which show vibrational frequencies below 200 cm<sup>-1</sup>. Modes between 150 and 160 cm<sup>-1</sup> were attributed to Te-Te vibrations as in amorphous Te in Refs. [1-4]. Modes between 175 and 195 cm<sup>-1</sup> have been attributed to As-Te vibrations [2-6]. Finally, modes between 230 and 240 cm<sup>-1</sup> have been attributed to amorphous As [3,5]. The mode whose frequency is around 195 cm<sup>-1</sup> is in good agreement with RS measurement in As<sub>2</sub>Se<sub>3</sub>, whose highest vibrational modes is around 250 cm<sup>-1</sup> [7] as already commented by Tverjanovich et al. [3]. These two modes scale perfectly with the square root masses of Se and Te, thus giving support to the assignment of the mode around 195 cm<sup>-1</sup> to the stretching vibrations of As-Te.

Visualization of the vibrational modes of  $\alpha$ -As<sub>2</sub>Te<sub>3</sub> at  $\Gamma$  calculated from *first principles* using the VASP code can be performed with the J-ICE software [8]. This visualization has allowed us to further understand the complex lattice dynamics of this compound as it was previously done for monoclinic  $\alpha$ -Bi<sub>2</sub>O<sub>3</sub> [9]. In general, we have observed that the motion of atoms is very complex and no modes related to isolated molecular units can be identified in monoclinic As<sub>2</sub>Te<sub>3</sub>. Modes with frequencies above 160 cm<sup>-1</sup> are dominated by the vibration of light As atoms; modes with frequencies between 100 and 150 cm<sup>-1</sup> are mainly determined by the vibration of heavy Te atoms; and modes with frequencies below 100 cm<sup>-1</sup> are collective or lattice modes of vibration where groups of As and Te atoms move in or out of phase. As matter of example **Fig. S1** shows the atomic vibrations in four Raman-active vibrational modes. The highest vibrational Raman mode Ag<sup>10</sup> mode shows the strong movement of As atoms in the *a-c* plane (**Fig. S1a**); the Ag<sup>7</sup> mode (**Fig. S1b**) corresponds to an almost pure vibration of Te atoms; the lowest Bg<sup>1</sup> mode (**Fig. S1c**) corresponds to a half shear mode between alternated layers with atoms vibrating along the *b* axis (note that the structure is shifted in this view to see the atom movements along the *b* axis perpendicular to *a* and *c* axis); and the Ag<sup>1</sup> mode (**Fig. S1d**) is the lowest-frequency Raman mode. In this complex monoclinic layered structure, there is no pure shear mode of the layers either in the *a-c* plane or along the *b* axis (either Raman or IR-active).

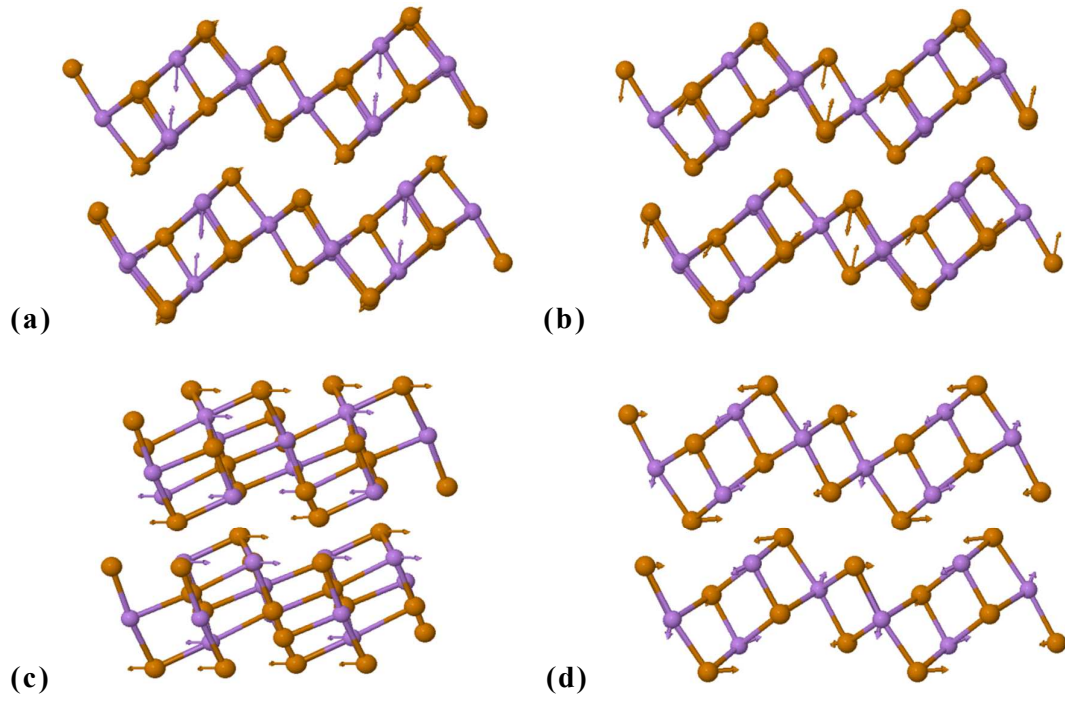


**Figure S1.** Scheme of atomic vibrations (As atoms are violet circles and Te atoms are orange circles) in some Raman-active vibrational modes of  $\alpha$ -As<sub>2</sub>Te<sub>3</sub>: (a) Ag<sup>10</sup> mode (optical mode of highest frequency), (b) Ag<sup>7</sup> mode (pure vibration of Te atoms), (c) Bg<sup>1</sup> mode (half shear mode along *b* axis), and (d) Ag<sup>1</sup> mode (optical mode of lowest frequency which is not a pure shear mode in the *a-c* plane).

Rietveld and LeBail analysis of HP-XRD measurements of  $\alpha$ -As<sub>2</sub>Te<sub>3</sub> under pressure

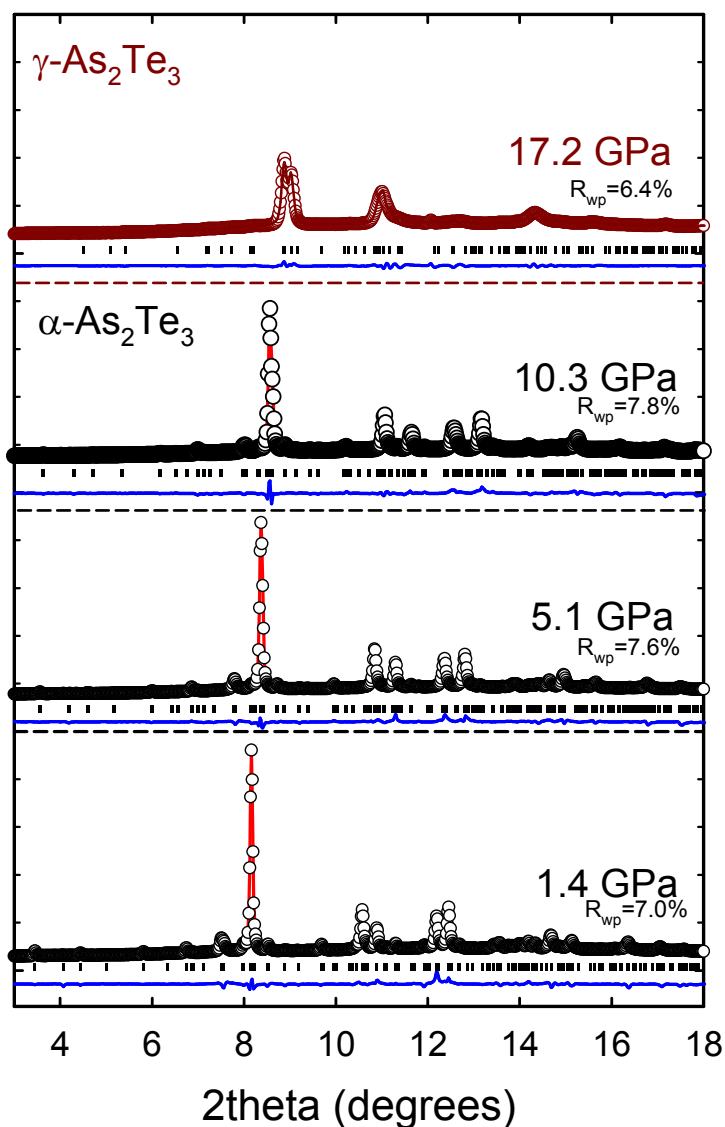


**Figure S2.** Rietveld refinement at two different pressures (1.4 and 5.1 GPa) and Le Bail refinement (10.3 GPa) for  $\alpha$ -As<sub>2</sub>Te<sub>3</sub>. Le Bail analysis for  $\gamma$ -As<sub>2</sub>Te<sub>3</sub> is also reported at 20 GPa. Experimental diffraction patterns are plotted as symbols, with the refined pattern as red lines and the residuals as blue lines. Vertical ticks represent theoretical position of the Bragg reflections both in  $\alpha$ -As<sub>2</sub>Te<sub>3</sub> and  $\gamma$ -As<sub>2</sub>Te<sub>3</sub>.

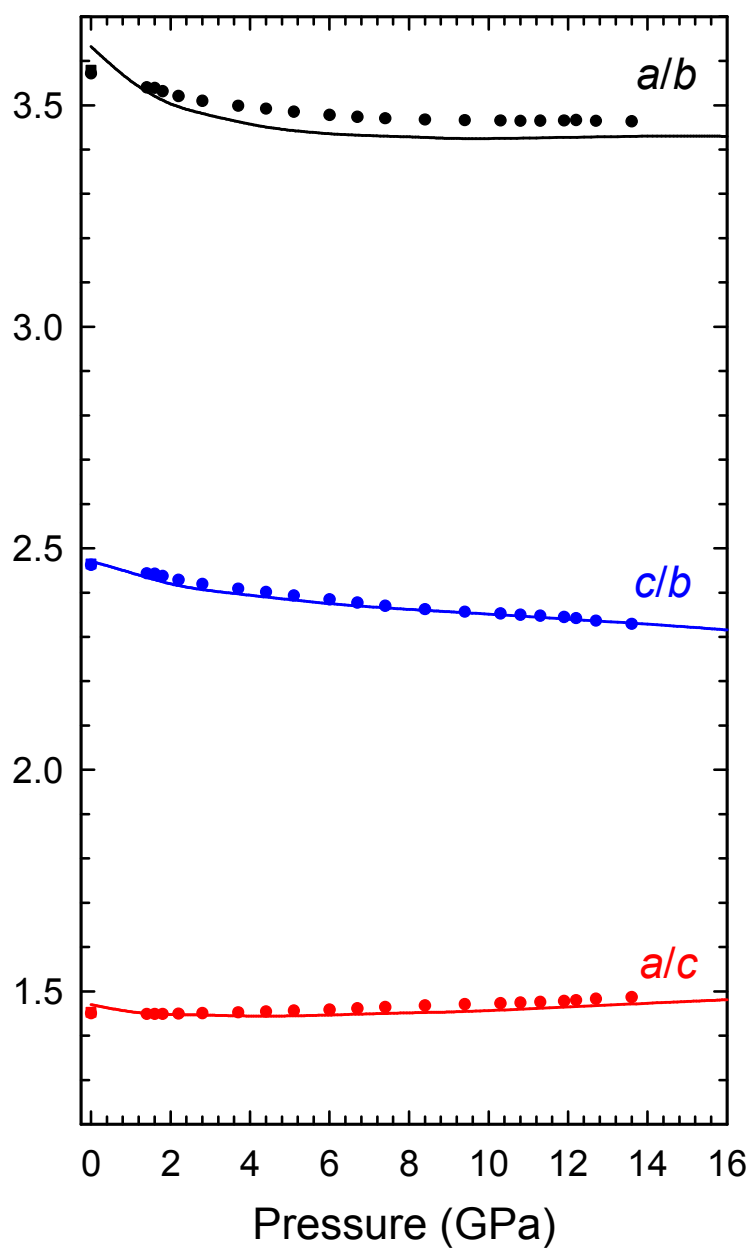


**Figure S3.** Experimental (symbols) and theoretical (solid lines) pressure dependence of the axial ratios of  $\alpha\text{-As}_2\text{Te}_3$  under compression. Squares correspond to data at ambient pressure taken from Ref. 10.

## Calculation of the experimental and theoretical compressibility tensor at different pressures

The isothermal compressibility tensor,  $\beta_{ij}$ , is a symmetric second rank tensor that relates the state of strain of a crystal to the change in pressure that induced it [11]. The tensor coefficients for a monoclinic crystal with  $b$  as the unique crystallographic axis are:

$$\beta_{ij} = \begin{pmatrix} \beta_{11} & 0 & \beta_{13} \\ 0 & \beta_{22} & 0 \\ \beta_{13} & 0 & \beta_{33} \end{pmatrix}$$

We have obtained the isothermal compressibility tensor coefficients for  $\alpha$ -As<sub>2</sub>Te<sub>3</sub> at several pressures using the IRE (Institute of Radio Engineers) convention for the orthonormal basis for the tensor:  $e_3 \parallel c$ ,  $e_2 \parallel b^*$ ,  $e_1 \parallel e_2 \times e_3$ . The tensor has been obtained with the finite Eulerian approximation as implemented in the Win\_Strain package [12].

The change of the  $\beta$  monoclinic angle (always perpendicular to the  $b$  axis) with pressure implies that, in this monoclinic compound, the direction of the  $a$  axis changes with pressure assuming both  $b$  and  $c$  axis constant. Furthermore, the departure of this monoclinic angle from 90° indicates that the direction of maximum compressibility is not exactly that of the  $a$  axis. Therefore, in order to evaluate the direction of maximum compressibility as a function of pressure we have calculated and diagonalised the experimental and theoretical isothermal compressibility tensor,  $\beta_{ij}$ , at different pressures.

The experimental and theoretical elements of this tensor at different pressures are reported in Tables S1 and S2, respectively, where the directions of the maximum, intermediate and minimum compressibility and the values of the compressibility along those directions are given by the eigenvectors ( $ev_i$ ,  $i=1-3$ ) and eigenvalues ( $\lambda_i$ ,  $i=1-3$ ), respectively.

First of all, we have to note that there is a reasonable good agreement between the experimental and calculated axial compressibilities ( $\beta_{ii}$  coefficients) at room pressure because  $\beta_{11} > \beta_{33} > \beta_{22}$  in both cases. A diagonalization of the  $\beta_{ij}$  tensor at room pressure yields for our experiments the maximum, intermediate and minimum compressibilities  $27.3(2.1) \cdot 10^{-3}$ ,  $14.0(1.1) \cdot 10^{-3}$  and  $4.7(4) \cdot 10^{-3}$  GPa<sup>-1</sup>, respectively; whereas for the case of our calculations the obtained values for the compressibilities are

$38(3) \cdot 10^{-3}$ ,  $14.6 (1.1) \cdot 10^{-3}$  and  $4.3(5) \cdot 10^{-3} \text{ GPa}^{-1}$ . These experimental (theoretical) results indicate that around 59% (67%) of the total compression at room pressure is being accommodated along the direction of maximum compressibility. Taking into account the eigenvector  $ev_1$ , the major compression direction at zero pressure occurs in the (0 1 0) plane at the given angle  $\Psi$  (see **Tables S1 and S2**) relative to the  $c$ -axis (from  $c$  to  $a$ ) or equivalently at an angle  $\theta$  relative to the  $a$ -axis (from  $a$  to  $c$ ). In particular, the experimental major compression direction at room pressure is at  $\theta = 16.0(1.4)^\circ$  from the  $a$ -axis whereas for our calculations is at  $5.5(7)^\circ$  from the  $a$ -axis. The direction of intermediate compressibility at room pressure given by eigenvector  $ev_2$  is in the (0 1 0) plane perpendicular to the direction of maximum compressibility, and the direction of minimum compressibility at room pressure given by eigenvector  $ev_3$  is along the  $b$  axis.

As regards the behaviour of the compressibility tensor under pressure, the most notable feature is that below 2.0 GPa the experimental compressibility of the  $a$ -axis is higher than that of the  $c$ -axis ( $\beta_{11} > \beta_{33}$ ); however, at 2.0 GPa both compressibilities are similar, and beyond 3.0 GPa  $\beta_{11} < \beta_{33}$  within experimental uncertainties. This behaviour is because the  $c$ -axis becomes more compressible than the  $a$ -axis above 3.0 GPa. Furthermore, the decrease of the compressibility of the  $a$  axis with increasing pressure is so large that the compressibilities of the  $a$  and  $b$  axes become equal around 13 GPa ( $\beta_{11} = \beta_{22}$ ). Correspondingly, the direction of maximum compressibility move away the  $a$ -axis and approaches the  $c$ -axis with increasing pressure; i.e., the  $\theta$  angle increases. At 3.0 GPa the direction of maximum compressibility is closer to the  $c$ -axis than to the  $a$ -axis and at pressures beyond 5 GPa the direction of maximum compressibility is already very close to the  $c$ -axis. Note that the results for the evolution of the theoretical tensor under pressure are similar to those obtained for the experimental tensor.

**Table S1.** Experimental isothermal compressibility tensor coefficients,  $\beta_{ij}$ , and their eigenvalues,  $\lambda_i$ , and eigenvectors,  $ev_i$ , for  $\alpha$ -As<sub>2</sub>Te<sub>3</sub> at several pressures. The results are given using the finite Eulerian method. The eigenvalues are given in decreasing value along a column.

P(GPa)	0.0	1.0	2.0	3.0	5.0	7.0	9.0	11.0	13.0
$\beta_{11}$ ( $10^{-3}$ GPa <sup>-1</sup> )	26.8 (2.0)	16.5 (1.2)	11.5 (8)	8.7 (6)	5.8 (5)	4.4 (4)	3.5 (3)	2.9 (3)	2.5 (3)
$\beta_{22}$ ( $10^{-3}$ GPa <sup>-1</sup> )	4.7 (5)	4.4 (4)	4.2 (3)	3.9 (3)	3.5 (3)	3.2 (3)	2.9 (3)	2.7 (3)	2.5 (4)
$\beta_{33}$ ( $10^{-3}$ GPa <sup>-1</sup> )	14.5 (1.1)	12.5 (9)	11.0 (8)	9.8 (7)	8.0 (6)	6.8 (5)	5.9 (4)	5.2 (4)	4.6 (4)
$\beta_{13}$ ( $10^{-3}$ GPa <sup>-1</sup> )	2.54 (22)	2.08 (18)	1.56 (15)	1.05 (12)	0.28 (9)	-0.11 (9)	-0.18 (9)	-0.07 (9)	0.04 (9)
$\lambda_1$ ( $10^{-3}$ GPa <sup>-1</sup> )	27.3 (2.1)	17.4 (1.3)	12.9 (9)	10.4 (8)	8.0 (6)	6.8 (5)	5.9 (4)	5.2 (4)	4.6 (4)
$ev_1$ ( $\lambda_1$ )	(0.98, 0.0, 0.19)	(0.92, 0.0, 0.39)	(0.76, 0.0, 0.65)	(0.52, 0.0, 0.85)	(0.12, 0.0, 0.99)	(0.07, 0.1, 1.00)	(0.05, 0.1, 1.00)	(0.03, 0.1, 1.00)	(0.02, 0.1, 1.00)
$\lambda_2$ ( $10^{-3}$ GPa <sup>-1</sup> )	14.0 (1.1)	11.6 (9)	9.7 (7)	8.1 (6)	5.8 (5)	4.4 (4)	3.4 (3)	2.9 (3)	2.5 (3)
$ev_2$ ( $\lambda_2$ )	(-0.19, 0, 0.98)	(-0.39, 0, 0.92)	(-0.65, 0, 0.76)	(-0.85, 0, 0.52)	(-0.99, 0, 0.12)	(-1.00, 0, 0.07)	(-1.00, 0, 0.05)	(-1.00, 0, 0.03)	(-1.00, 0, 0.02)
$\lambda_3$ ( $10^{-3}$ GPa <sup>-1</sup> )	4.7 (4)	4.4 (4)	4.2 (3)	3.9 (3)	3.5 (3)	3.2 (3)	2.9 (3)	2.7 (3)	2.5 (3)
$ev_3$ ( $\lambda_3$ )	(0, 1, 0)	(0, 1, 0)	(0, 1, 0)	(0, 1, 0)	(0, 1, 0)	(0, 1, 0)	(0, 1, 0)	(0, 1, 0)	(0, 1, 0)
$\Psi, \theta$ (°) <sup>a</sup>	78.8 (1.4), 16.0 (1.4)	66.9 (1.2), 28.2 (1.2)	49.6 (2.3), 45.7 (2.3)	31.4 (2.9), 63.9 (2.9)	7.1 (2.4), 88.5 (2.4)	-2.6 (2.3), 98.2 (2.3)	-4.2 (2.3), 99.7 (2.3)	-1.6 (2.4), 97.0 (2.4)	1.1 (2.4), 94.3 (2.4)

<sup>a</sup> The major compression direction occurs in the (0 1 0) plane at the given angles  $\Psi$  to the  $c$ -axis (from  $c$  to  $a$ ) and  $\theta$  to the  $a$ -axis (from  $a$  to  $c$ ).

**Table S2.** Theoretical isothermal compressibility tensor coefficients,  $\beta_{ij}$ , and their eigenvalues,  $\lambda_i$ , and eigenvectors,  $ev_i$ , for  $\alpha$ -As<sub>2</sub>Te<sub>3</sub> at several pressures. The results are given using the finite Eulerian method. The eigenvalues are given in decreasing value along a column.

P(GPa)	0.0	1.0	3.0	4.0	5.0	7.0	9.0	11.0	13.0
$\beta_{11}$ ( $10^{-3}$ GPa <sup>-1</sup> )	38 (3)	21.4 (1.6)	10.4 (7)	8.2 (6)	6.7 (5)	4.9 (4)	3.9 (3)	3.2 (3)	2.7 (2)
$\beta_{22}$ ( $10^{-3}$ GPa <sup>-1</sup> )	4.3 (5)	4.2 (4)	3.9 (3)	3.8 (3)	3.7 (3)	3.5 (3)	3.3 (3)	3.2 (4)	3.0 (4)
$\beta_{33}$ ( $10^{-3}$ GPa <sup>-1</sup> )	14.6 (1.1)	12.7 (9)	10.0 (7)	9.0 (6)	8.2 (6)	6.9 (5)	6.0 (4)	5.3 (4)	4.8 (4)
$\beta_{13}$ ( $10^{-3}$ GPa <sup>-1</sup> )	-0.14 (2)	0.93 (9)	0.95 (9)	0.53 (7)	-0.005 (9)	-0.34 (7)	-0.43 (7)	-0.54 (7)	-0.63 (8)
$\lambda_1$ ( $10^{-3}$ GPa <sup>-1</sup> )	38(3)	21.5 (1.6)	11.2 (8)	9.2 (7)	8.2 (6)	7.0 (5)	6.1 (4)	5.4 (4)	4.9 (4)
$ev_1$ ( $\lambda_1$ )	(1.00, 0, 0.01)	(0.99, 0, 0.11)	(0.79, 0, 0.62)	(0.46, 0, 0.89)	(0.00, 0, 1.00)	(0.16, 0, -0.99)	(0.19, 0, -0.98)	(0.23, 0, -0.97)	(0.27, 0, -0.96)
$\lambda_2$ ( $10^{-3}$ GPa <sup>-1</sup> )	14.6 (1.1)	12.6 (9)	9.2 (7)	7.9 (6)	6.7 (5)	4.9 (4)	3.8 (3)	3.2 (7)	3.0 (4)
$ev_2$ ( $\lambda_2$ )	(0.01, 0, 1.00)	(0.11, 0, -0.99)	(0.62, 0, -0.79)	(0.89, 0, -0.46)	(1.00, 0, 0.00)	(0.99, 0, 0.16)	(0.98, 0, 0.19)	(0.97, 0, 0.23)	(0.96, 0, 0.27)
$\lambda_3$ ( $10^{-3}$ GPa <sup>-1</sup> )	4.3 (5)	4.2 (4)	3.9 (3)	3.8 (3)	3.7 (3)	3.5 (3)	3.3 (3)	3.1 (5)	2.5 (2)
$ev_3$ ( $\lambda_3$ )	(0, 1, 0)	(0, 1, 0)	(0, 1, 0)	(0, 1, 0)	(0, 1, 0)	(0, 1, 0)	(0, 1, 0)	(0, 1, 0)	(0, 1, 0)
$\Psi, \theta$ (°) <sup>a</sup>	90.3 (7), 5.5 (7)	84.0 (5), 12.0 (5)	51.9 (1.9), 44.4 (1.9)	27.1 (2.8), 69.3 (2.8)	-0.2 (1.6), 96.6 (2.5)	-9.4 (1.7), 105.7 (1.7)	-11.1 (1.6), 107.3 (1.6)	-13.6 (1.7), 109.6 (1.7)	-15.9 (1.8), 111.8 (1.8)

<sup>a</sup> The major compression direction occurs in the (0 1 0) plane at the given angles  $\Psi$  to the  $c$ -axis (from  $c$  to  $a$ ) and  $\theta$  to the  $a$ -axis (from  $a$  to  $c$ ).



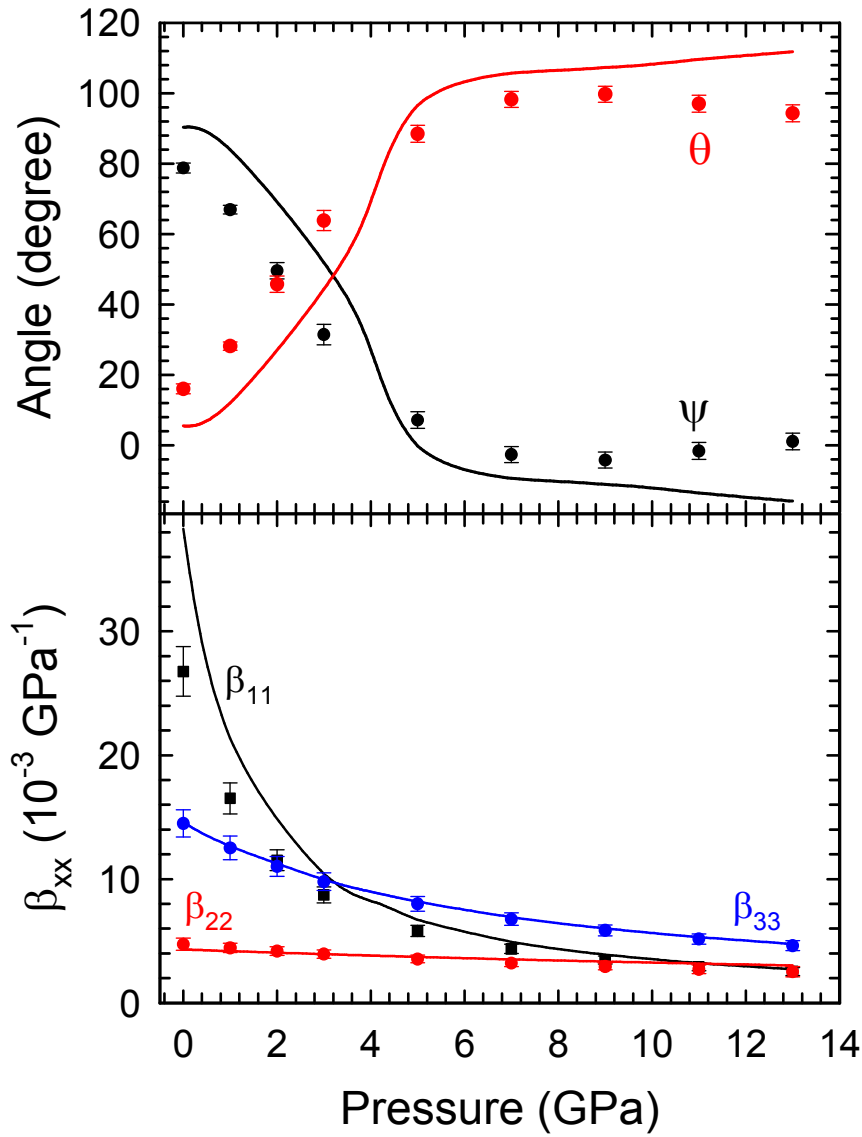


**Figure S4.** (a) Angle of maximum compressibility  $\psi$  relative to the  $c$ -axis (from  $c$  to  $a$ ) or equivalently  $\theta$  relative to the  $a$ -axis (from  $a$  to  $c$ ). (b)  $\beta_{xx}$  coefficients of the compressibility tensor that indicates the compressibility along the crystallographic axis. Solid lines represent the *ab initio* calculations and symbols data obtained from our experiments.

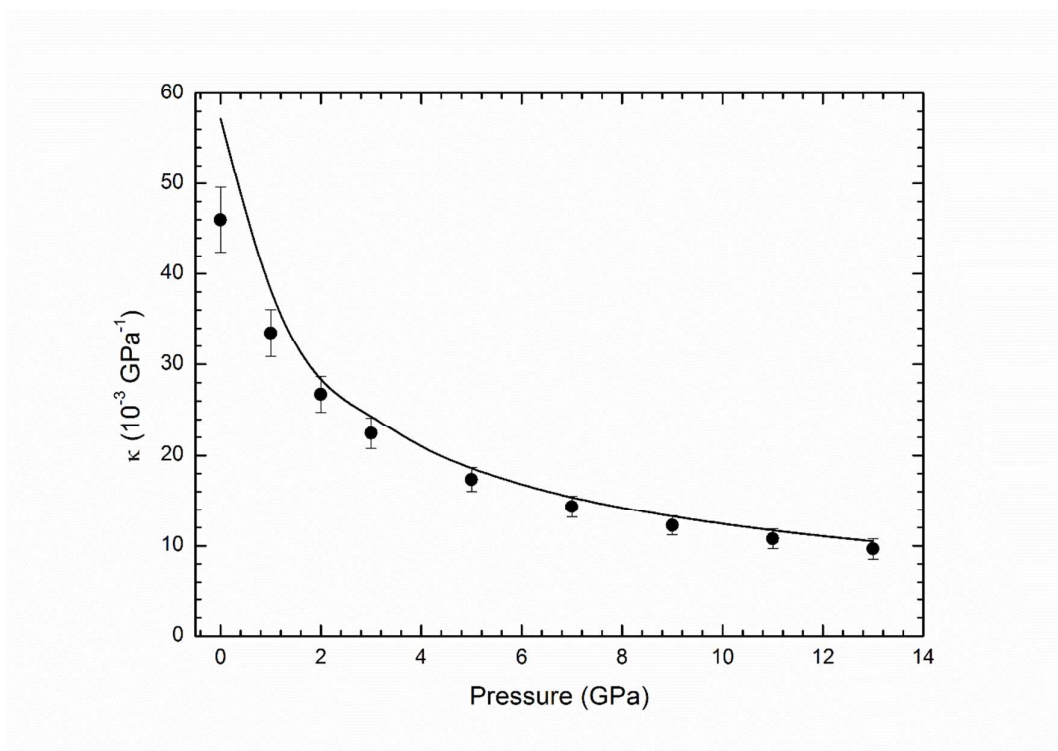


**Figure S5.** Experimental (symbols) and theoretical (curve) pressure dependence of the volume compressibility as obtained from the trace of the experimental and theoretical compressibility tensors at different pressures.

### Pressure dependence of atomic coordinates and interatomic distances

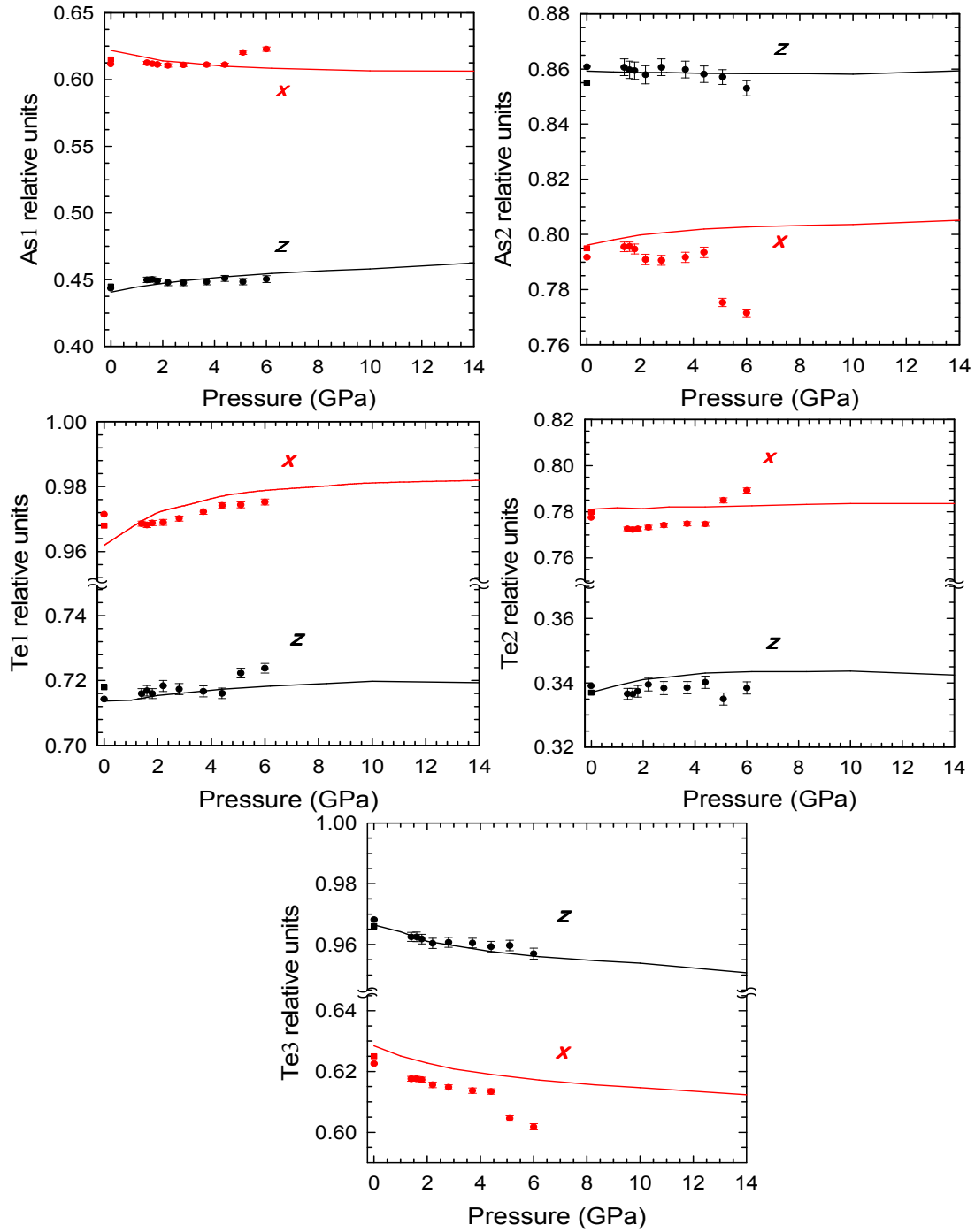


**Figure S6.** Pressure dependence of the experimental (symbols) and theoretical (lines) As1, As2, Te1, Te2 and Te3 x and z coordinates in  $\alpha$ -As<sub>2</sub>Te<sub>3</sub>. Squares correspond to data at ambient pressure taken from Ref. 10.

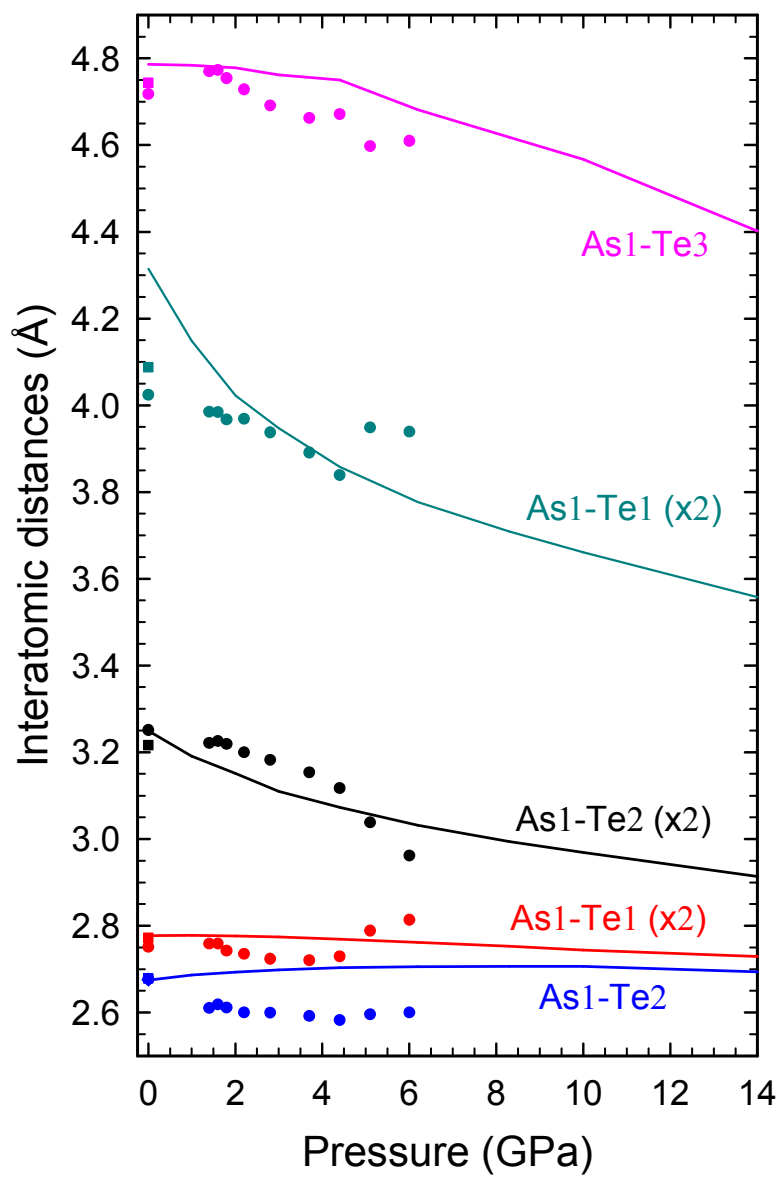


**Figure S7.** Pressure dependence of the experimental (symbols) and theoretical (lines) As1-Te distances. Squares correspond to data at ambient pressure taken from Ref. 10.

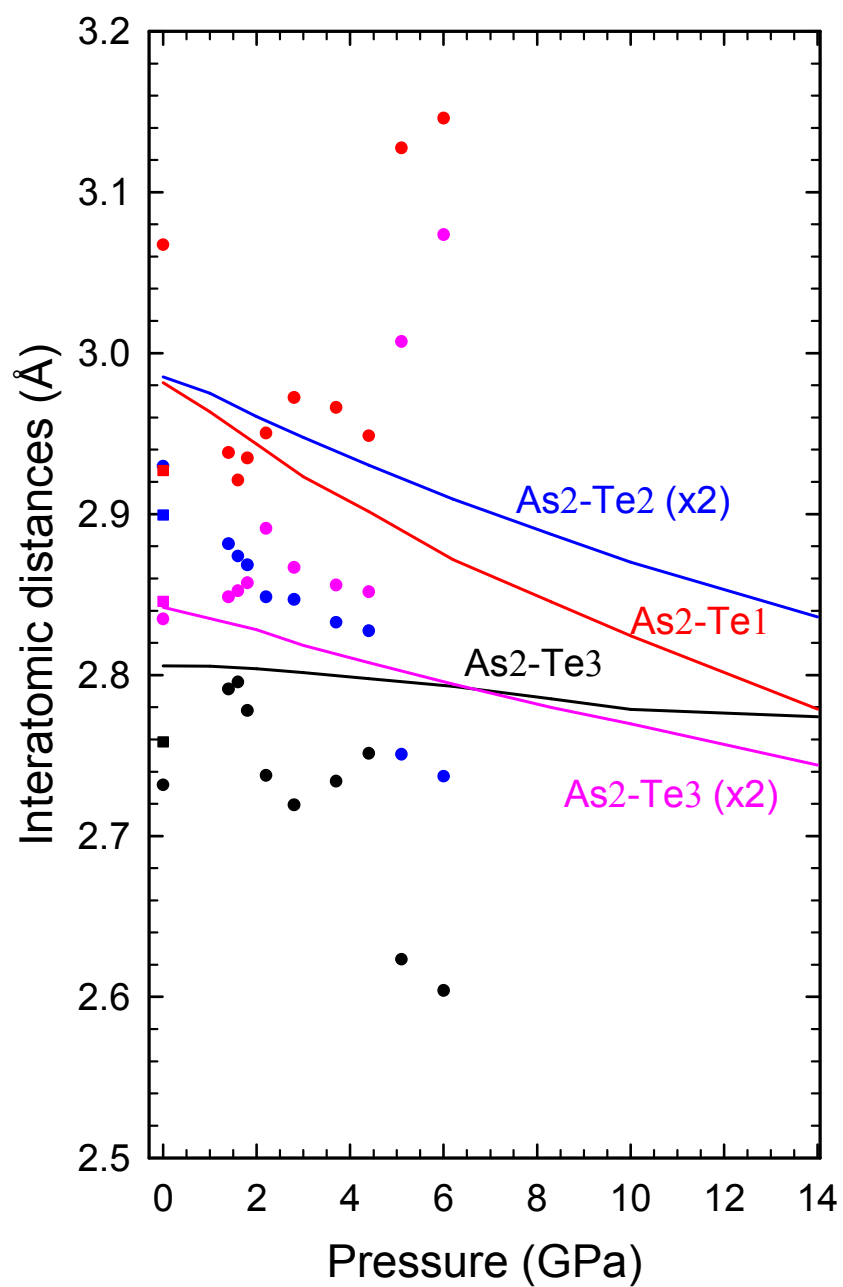


**Figure S8.** Pressure dependence of the experimental (symbols) and theoretical (lines) As<sub>2</sub>-Te distances. Squares correspond to data at ambient pressure taken from Ref. 10.

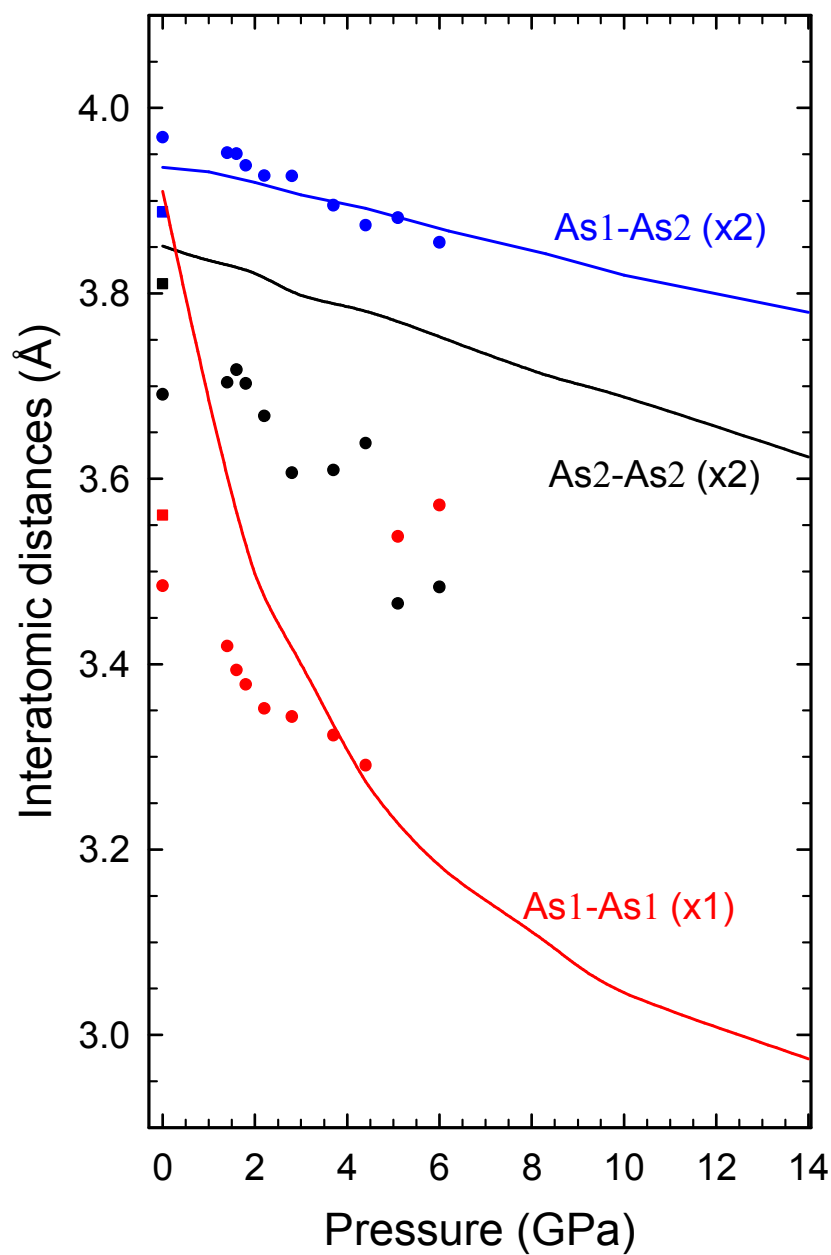


**Figure S9.** Pressure dependence of the experimental (symbols) and theoretical (lines) As-As distances. Squares correspond to data at ambient pressure taken from Ref. 10.

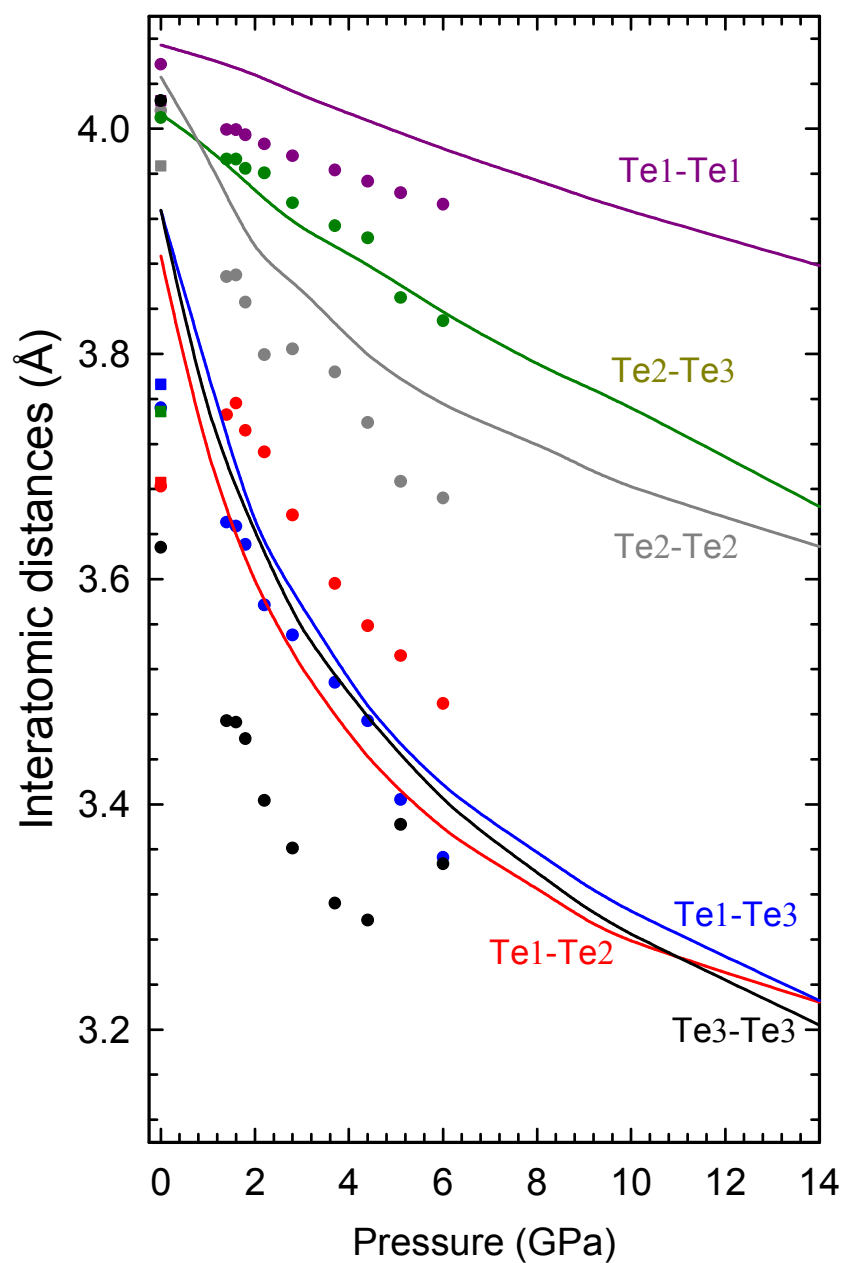


**Figure S10.** Pressure dependence of the experimental (symbols) and theoretical (lines) Te-Te distances. Squares correspond to data at ambient pressure taken from Ref. 10.

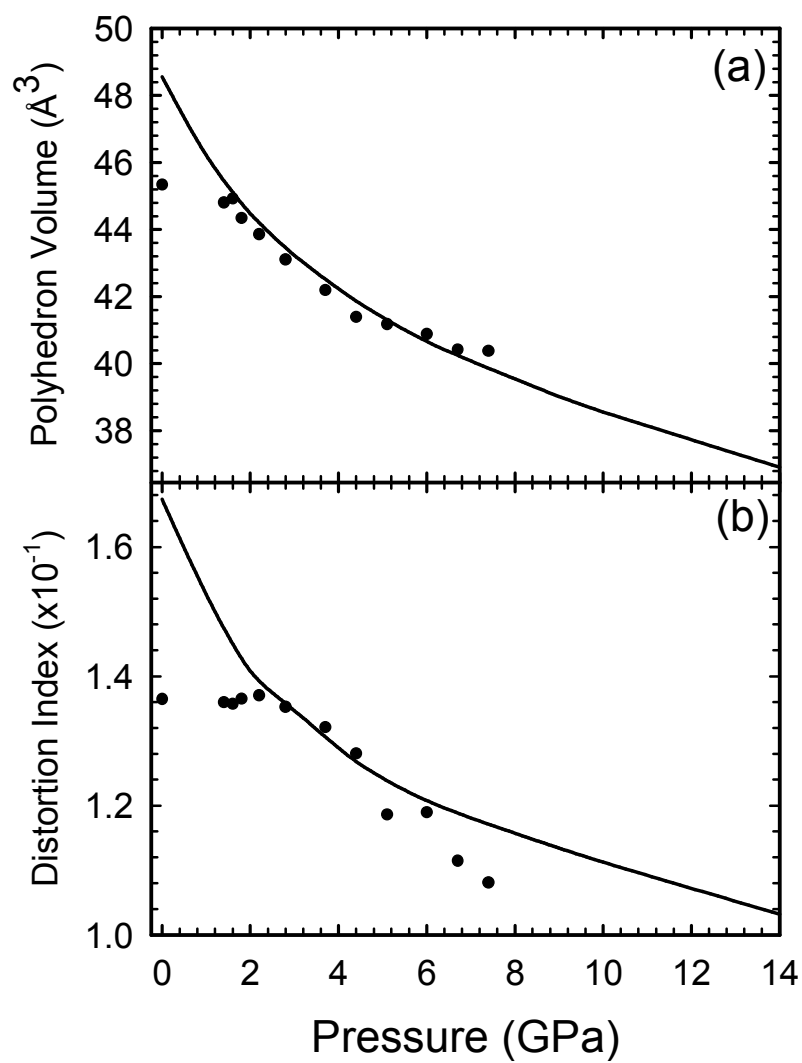


**Figure S11.** Pressure dependence of the experimental (symbols) and theoretical (lines) volume (a) and distortion index (b) of the As1 polyhedron.



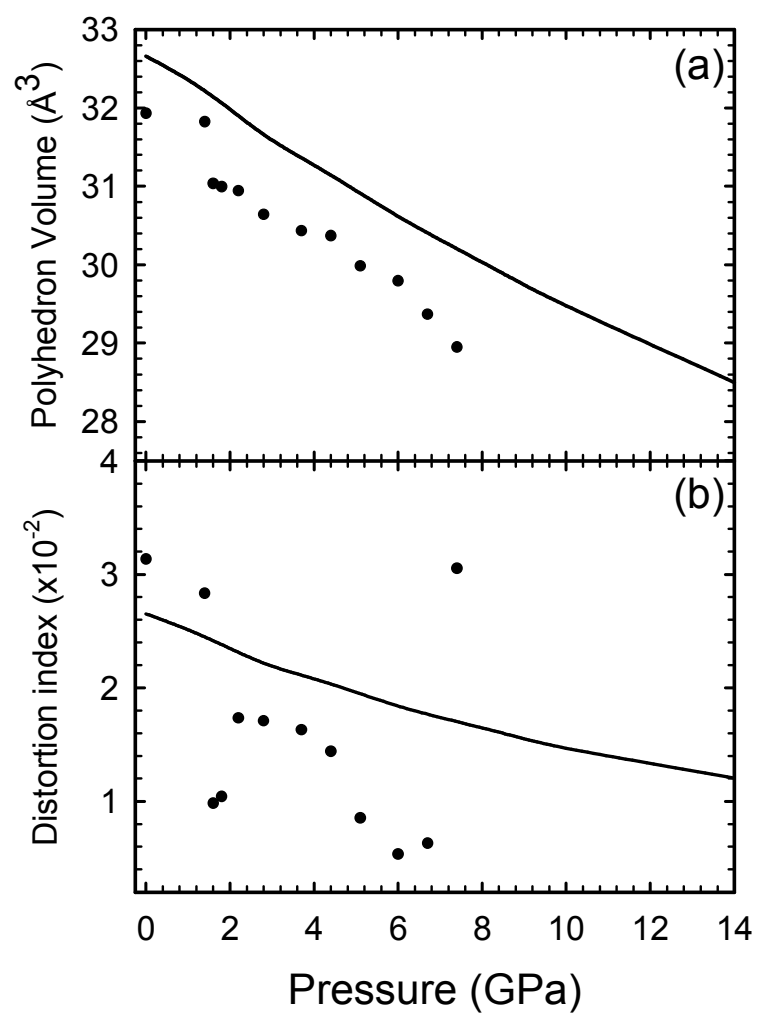


**Figure S12.** Pressure dependence of the experimental (symbols) and theoretical (lines) volume (a) and distortion index (b) of the As<sub>2</sub> polyhedron.

### Comparison of the structure of $\alpha$ -As<sub>2</sub>Te<sub>3</sub> and its pressure behavior with other related group-15 sesquichalcogenides

It is interesting to compare the structure of  $\alpha$ -As<sub>2</sub>Te<sub>3</sub> and its pressure behavior with that of other group-15 sesquioxides and sesquichalcogenides in order to understand the role played by the As LEP in the structure of  $\alpha$ -As<sub>2</sub>Te<sub>3</sub>. **Table S3** summarizes the experimental and theoretical BM-EoS of  $\alpha$ -As<sub>2</sub>Te<sub>3</sub>,  $\alpha$ -Sb<sub>2</sub>Te<sub>3</sub>,  $\alpha$ -Bi<sub>2</sub>Te<sub>3</sub> and orthorhombic Sb<sub>2</sub>Se<sub>3</sub>. As observed, the bulk modulus of  $\alpha$ -As<sub>2</sub>Te<sub>3</sub> is smaller than those of  $\alpha$ -Sb<sub>2</sub>Te<sub>3</sub> and  $\alpha$ -Bi<sub>2</sub>Te<sub>3</sub>. This result is in good agreement with the larger activity of the LEP in As than in Sb and Bi tellurides and how this activity favors open structures with a large compressibility. In this way, it is easy to understand that the increase of the cation LEP activity in the series Bi-Sb-As explains that distorted structures caused by the cation LEP are present in Bi<sub>2</sub>X<sub>3</sub> ( $X = \text{O, S}$ ), Sb<sub>2</sub>X<sub>3</sub> ( $X = \text{O, S, Se}$ ) and As<sub>2</sub>X<sub>3</sub> ( $X = \text{O, S, Se, Te}$ ) since cation LEP activity is different for different anions [31]. The comparison of compounds with the same anion, shows that the volume per unit formula rises when the atomic number of the cation increases, as expected by the increase of the cationic radius size. However, the LEP effect softens this increase allowing a small increment of the initial volume of  $\alpha$ -As<sub>2</sub>Te<sub>3</sub> compared with that observed in  $\alpha$ -Sb<sub>2</sub>Te<sub>3</sub>. On the other hand, the bulk modulus of  $\alpha$ -As<sub>2</sub>Te<sub>3</sub> is similar to that of Sb<sub>2</sub>Se<sub>3</sub>.

It is also worthy to compare the compressibility of the different axes in these compounds (see **Table S4**). The experimental compressibility of the  $a$ -axis at room pressure in  $\alpha$ -As<sub>2</sub>Te<sub>3</sub> ( $26.8(2) \cdot 10^{-3} \text{ GPa}^{-1}$ ) can be compared to that of the  $c$ -axis in  $\alpha$ -Sb<sub>2</sub>Te<sub>3</sub> (around  $21.2 \cdot 10^{-3} \text{ GPa}^{-1}$ ) [85] and  $\alpha$ -Bi<sub>2</sub>Te<sub>3</sub> (around  $15.2 \cdot 10^{-3} \text{ GPa}^{-1}$ ) [89] since layers are mainly stacked along these directions in the different compounds. As observed, the interlayer compressibility of  $\alpha$ -As<sub>2</sub>Te<sub>3</sub> is larger than of  $\alpha$ -Sb<sub>2</sub>Te<sub>3</sub> and  $\alpha$ -Bi<sub>2</sub>Te<sub>3</sub>. Again, this result is in good agreement with the larger Te-Te interlayer distance observed in As telluride than in Sb and Bi tellurides as expected by the larger cation LEP activity of As than of Sb and Bi for the same anion. On the contrary, the intralayer compressibility at room pressure, which is mainly that of  $b$ -axis in  $\alpha$ -As<sub>2</sub>Te<sub>3</sub> ( $4.7(5) \cdot 10^{-3} \text{ GPa}^{-1}$ ) and that of  $a$ -axis in  $\alpha$ -Sb<sub>2</sub>Te<sub>3</sub> ( $6.2 \cdot 10^{-3} \text{ GPa}^{-1}$ ) [19] and  $\alpha$ -Bi<sub>2</sub>Te<sub>3</sub> ( $8.4 \cdot 10^{-3} \text{ GPa}^{-1}$ ) [24] are smaller than those of the other axes in the three compounds, as expected for the intralayer strong covalent  $A$ -Te ( $A = \text{As, Sb, Bi}$ ) bonds.

An even closer comparison of axial compressibilities can be performed between  $\alpha$ -As<sub>2</sub>Te<sub>3</sub> and Sb<sub>2</sub>Se<sub>3</sub> since the latter compound crystallizes in an orthorhombic layered

structure (*Pnma* space group) isostructural to  $\text{Sb}_2\text{S}_3$  and  $\text{Bi}_2\text{S}_3$  and with similar tendency than  $\alpha\text{-As}_2\text{Te}_3$  to form needles extended along the *b*-axis which are weakly linked to form extended layers. The structure of  $\text{Sb}_2\text{Se}_3$  is more distorted than that of  $\alpha\text{-As}_2\text{Te}_3$  and has also two independent cations, Sb1 and Sb2. At room pressure, both cations are bonded to three Se atoms with short bonds ( $< 2.7 \text{ \AA}$ ) and to four additional Se atoms with longer bonds ( $> 3.0 \text{ \AA}$ ), giving rise to an apparent sevenfold coordination. Actually, the coordination at ambient pressure is much smaller. The shortest bonds give rise to distorted trigonal Sb1Se3 units and tetragonal Sb2Se5 pyramids, thus resulting in Sb1Se3E tetrahedra and Sb2Se5E octahedra (where E indicates the LEP of both Sb atoms) of quasi-fourfold and quasi-sixfold coordination, respectively. Similarly to  $\text{Sb}_2\text{Se}_3$ , the polyhedral units of  $\alpha\text{-As}_2\text{Te}_3$  could be described as As1Te5E octahedra and As2Te6 octahedra. From this perspective, it is observed that the cation LEP is active in both polyhedral units of  $\text{Sb}_2\text{Se}_3$ , but only in one polyhedral unit of  $\alpha\text{-As}_2\text{Te}_3$ ; i.e., the LEP activity of Sb in  $\text{Sb}_2\text{Se}_3$  is larger than that of As in  $\alpha\text{-As}_2\text{Te}_3$ . This different LEP activity is a consequence that the cation LEP activity depends on the anion and increases for lighter anions as already reported elsewhere [31].

Due to the larger cation LEP activity in  $\text{Sb}_2\text{Se}_3$  than in  $\alpha\text{-As}_2\text{Te}_3$ , the zigzag layers in  $\text{Sb}_2\text{Se}_3$  are cut along the *c*-axis [32]. Inside the needles extended along the *b*-axis, intralayer Sb-Se distances are around  $2.67 \text{ \AA}$ ; a value similar to that of most intralayer As-Te bonds (**Figs. S6 and S7**). These needles are separated from adjacent ones in a zigzag way by intermediate primary and secondary interchain distances (around  $3.1 \text{ \AA}$ ) mainly along the *c*-axis. Finally, the layers formed by linked chains along *b* and *c* axes pile up along the *a*-axis with large distances between layers (around  $3.7 \text{ \AA}$ ) [32]. In this way, the structure of  $\text{Sb}_2\text{Se}_3$  results in a *b* lattice parameter around  $4 \text{ \AA}$ , similar to that of  $\alpha\text{-As}_2\text{Te}_3$ , while *a* and *c* lattice parameters are around  $11.8 \text{ \AA}$  and  $11.6 \text{ \AA}$ , respectively. The compressibilities of *a*, *b* and *c* axes in  $\text{Sb}_2\text{Se}_3$  at room pressure are around  $13.6 \cdot 10^{-3}$ ,  $5.0 \cdot 10^{-3}$  and  $9.3 \cdot 10^{-3} \text{ GPa}^{-1}$  [30] so they clearly scale with the lattice parameter values and with the Sb-Se distances along the different directions. This situation is the same already described for  $\alpha\text{-As}_2\text{Te}_3$  where the compressibility of the *a*, *b* and *c* axes at room pressure scale with the lattice parameters and with the interlayer Te-Te distance (around  $3.8 \text{ \AA}$ ), with the intralayer As2-Te distances (around  $2.8 \text{ \AA}$ ), and with the intralayer As1-Te distance (around  $3.2 \text{ \AA}$ ). The largest difference in axial compressibilities between  $\alpha\text{-As}_2\text{Te}_3$  and  $\text{Sb}_2\text{Se}_3$  occurs along the *a*-axis. This result

must be ascribed to the different compressibility of van der Waals interlayer Te-Te distances than Se-Se distances since all three tellurides show larger interlayer compressibilities than the selenide  $\text{Sb}_2\text{Se}_3$ .

In summary, the structure of  $\alpha\text{-As}_2\text{Te}_3$  can be understood as intermediate between that of  $\alpha\text{-Sb}_2\text{Te}_3$  and  $\text{Sb}_2\text{Se}_3$  in good agreement with what is expected from the activity of cation LEP in group-15 sesquichalcogenides.

Compound	$V_0$ ( $\text{\AA}^3$ )	$B_0$	$B_0'$	Character
$\alpha\text{-As}_2\text{Te}_3$	144.8	24	7.9	Exp <sup>a</sup>
	143.0	26	9.0	Exp <sup>b</sup>
	143.0	33	4.0(fixed)	Exp <sup>b</sup>
	142.6	38.4	4.0(fixed)	Exp <sup>c</sup>
	150.8	19.7	8.1	The <sup>a</sup>
	138.4	42.7		The <sup>d</sup>
$\alpha\text{-Sb}_2\text{Te}_3$	159.7	40	4 (fixed)	Exp <sup>e</sup>
	159.7	30.2	9.4	Exp <sup>f</sup>
		45	4 (fixed)	Exp <sup>g</sup>
	159.9	36.1	6.2	Exp <sup>h</sup>
	157.5	54.7	4	Exp <sup>i</sup>
	158.1	41.0	5.2	The <sup>j</sup>
	159.9	33.1		The <sup>k</sup>
$\alpha\text{-Bi}_2\text{Te}_3$	169.2	56.2	2.1	Exp <sup>l</sup>
		21.9*	17.1	Exp <sup>l</sup>
		38.2**	4.6	
	168.5	28.1*	13.8	Exp <sup>m</sup>
	168.5	36.3**	5.5	
	170.0	46.3	3.6	Exp <sup>n</sup>
		50.1	3.0	Exp <sup>o</sup>
	166.7	41.6	4.68	The <sup>p</sup>
	168.8	28.1		The <sup>q</sup>
		40.3		The <sup>r</sup>
$\text{Sb}_2\text{Se}_3$	136.4	30	6.1	Exp <sup>q</sup>

<sup>a</sup> This work, <sup>b</sup> Ref. 13, <sup>c</sup> Ref. 14, <sup>d</sup> Ref. 15, <sup>e</sup> Ref. 16, <sup>f</sup> Ref. 17, <sup>g</sup> Ref. 18, <sup>h</sup> Ref. 19, <sup>i</sup> Ref. 20, <sup>j</sup> Ref. 21, <sup>k</sup> Ref. 22, <sup>l</sup> Ref. 23, <sup>m</sup> Ref. 24, <sup>n</sup> Ref. 25, <sup>o</sup> Ref. 26, <sup>p</sup> Ref. 27, <sup>q</sup> Ref. 28, <sup>r</sup> Ref. 29, <sup>q</sup> Ref. 30. \* Values below 3 GPa. \*\* Values above 3 GPa.

**Table S3.** Experimental (Exp) and theoretical DFT-GGA (The) parameters of the BM-EoS of  $\alpha\text{-As}_2\text{Te}_3$ ,  $\alpha\text{-Sb}_2\text{Te}_3$ ,  $\alpha\text{-Bi}_2\text{Te}_3$  and  $\text{Sb}_2\text{Se}_3$  at ambient pressure. Volumes per formula unit are taken for comparison of the different compounds.

Compound	$a$	$\chi_a$	$B$	$\chi_b$	$c$	$\chi_c$
$\alpha$ -As <sub>2</sub> Te <sub>3</sub> <sup>a</sup>	14.55	26.8	4.03	4.7	9.96	14.5
Sb <sub>2</sub> Se <sub>3</sub> <sup>b</sup>	11.80	13.6	3.98	5.0	11.60	9.3
$\alpha$ -Sb <sub>2</sub> Te <sub>3</sub> <sup>c</sup>	4.27	6.2	4.27	6.2	15.19	21.2
$\alpha$ -Bi <sub>2</sub> Te <sub>3</sub> <sup>d</sup>	4.38	8.4	4.38	8.4	15.18	15.2

<sup>a</sup> This work, <sup>b</sup> Ref. 30, <sup>c</sup> Ref. 19, <sup>d</sup> Ref. 24.

**Table S4.** Lattice parameters (in Å) and compressibilities (in 10<sup>-3</sup> GPa<sup>-1</sup>) of  $\alpha$ -As<sub>2</sub>Te<sub>3</sub>,  $\alpha$ -Sb<sub>2</sub>Te<sub>3</sub>,  $\alpha$ -Bi<sub>2</sub>Te<sub>3</sub> and Sb<sub>2</sub>Se<sub>3</sub> at ambient pressure. Values with same shadow color correspond to distances and compressibilities to be compared. Note that  $c$  lattice parameter of  $\alpha$ -Sb<sub>2</sub>Te<sub>3</sub> and  $\alpha$ -Bi<sub>2</sub>Te<sub>3</sub> has been divided by 2 because there are two times more layers along the unit cell of these compounds than along the  $a$ -axis of  $\alpha$ -As<sub>2</sub>Te<sub>3</sub> and Sb<sub>2</sub>Se<sub>3</sub>.

*Ab-initio* calculations of enthalpy vs pressure

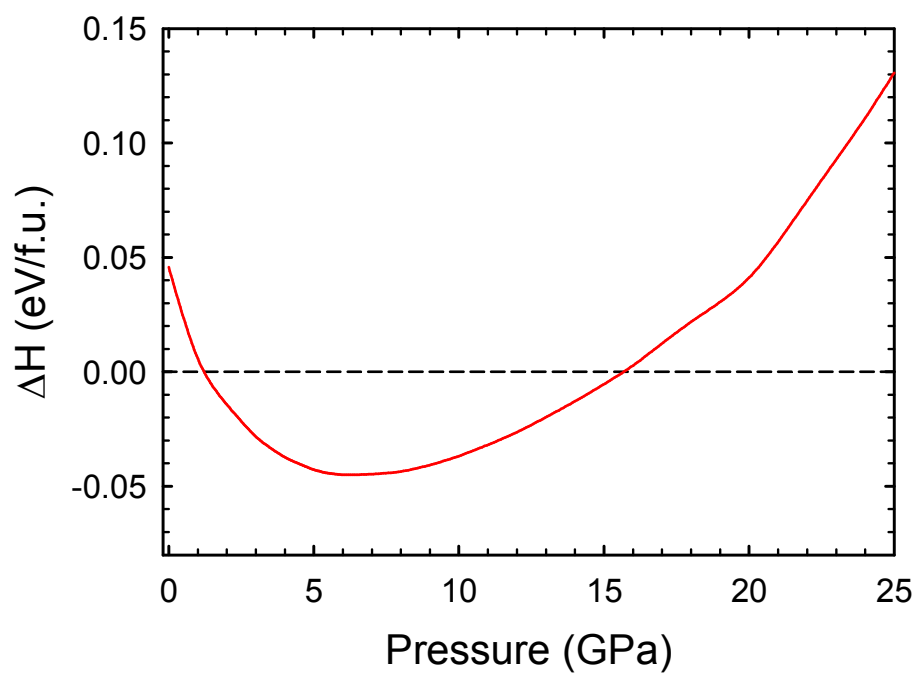


**Figure S13.** Enthalpy difference curves of the  $\alpha$  (black dashed line) and  $\beta$  (red solid line) phases as a function of pressure with respect to the  $\alpha$ -phase which has been taken as a reference.

# Vibrational properties of $\alpha$ -As<sub>2</sub>Te<sub>3</sub> at high pressures

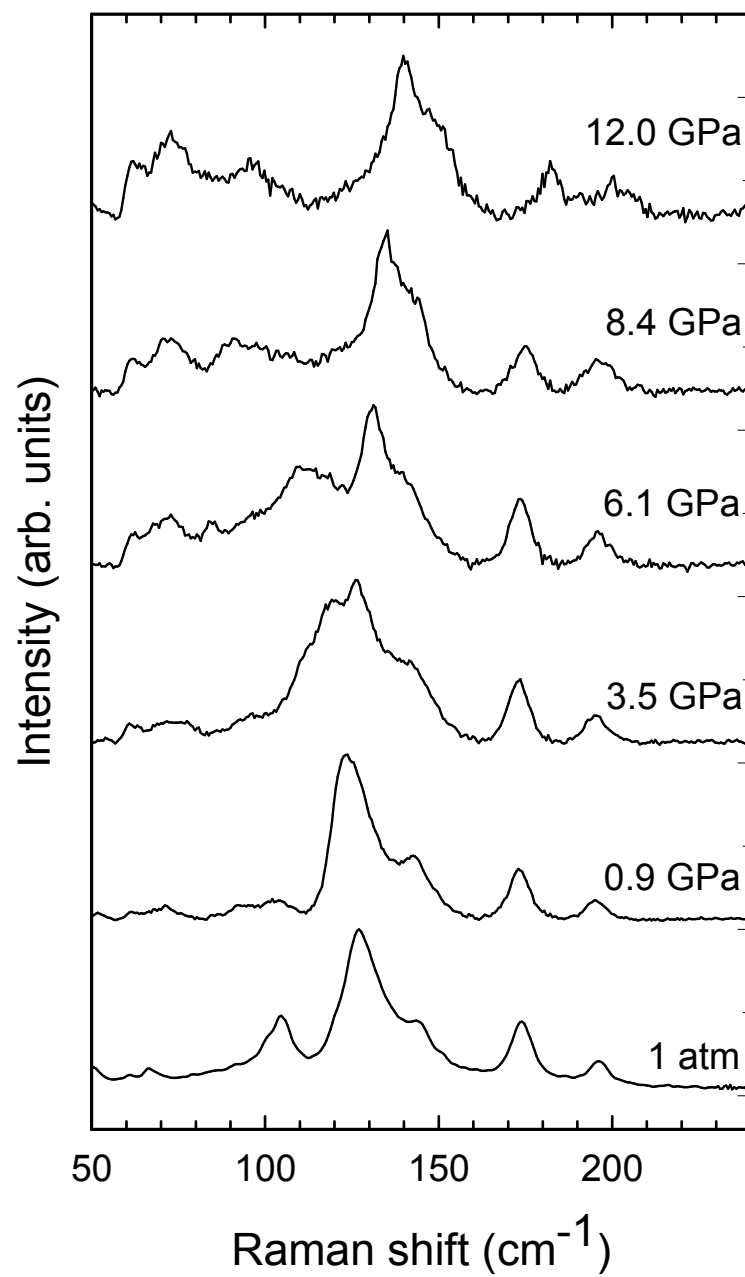


**Figure S14.** Room-temperature Raman spectra of  $\alpha$ -As<sub>2</sub>Te<sub>3</sub> at selected pressures under non-hydrostatic conditions.



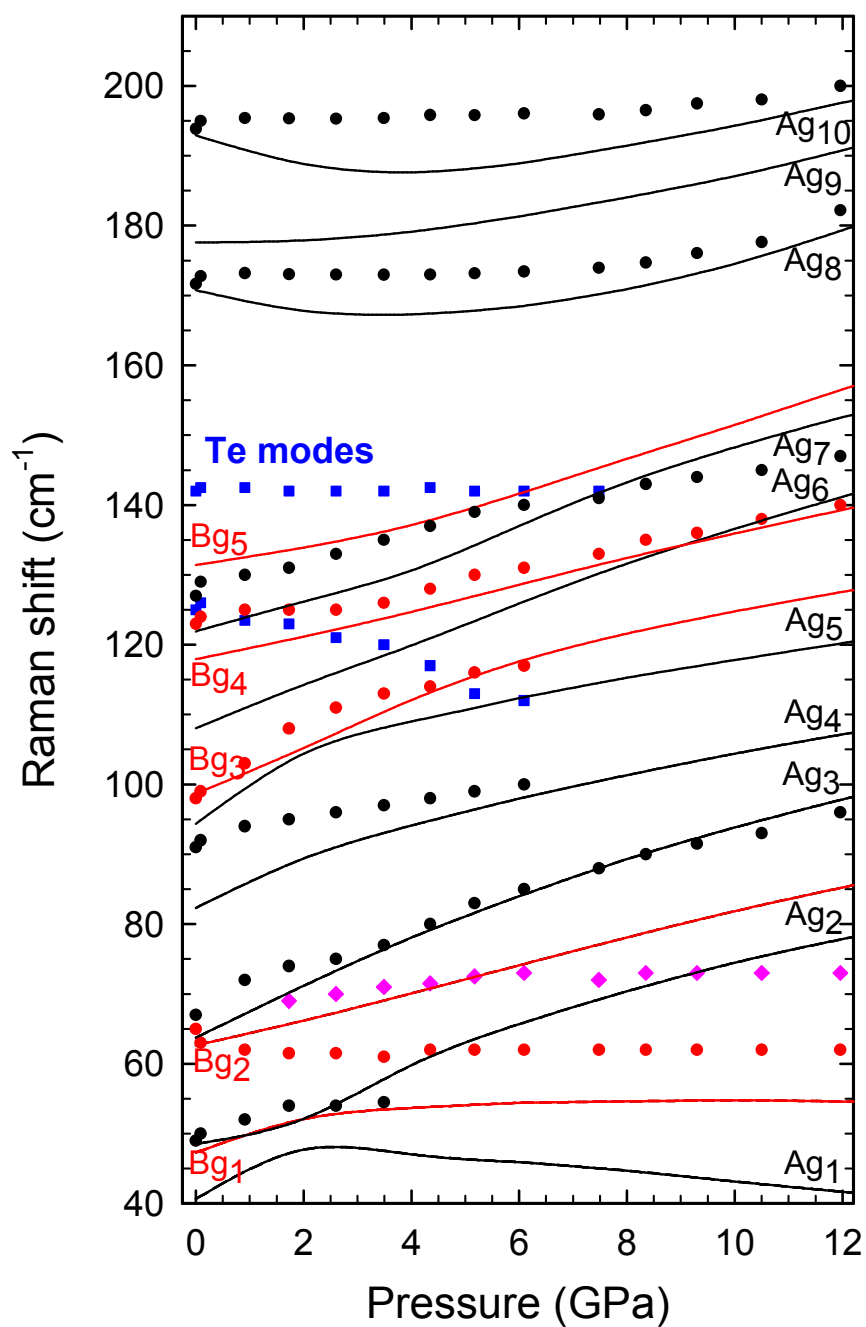


**Figure S15.** Experimental (symbols) and theoretical (lines) pressure dependence of the Raman-mode frequencies of  $\alpha$ -As<sub>2</sub>Te<sub>3</sub> under non-hydrostatic conditions. Different colors represent Raman-active modes of different symmetries.

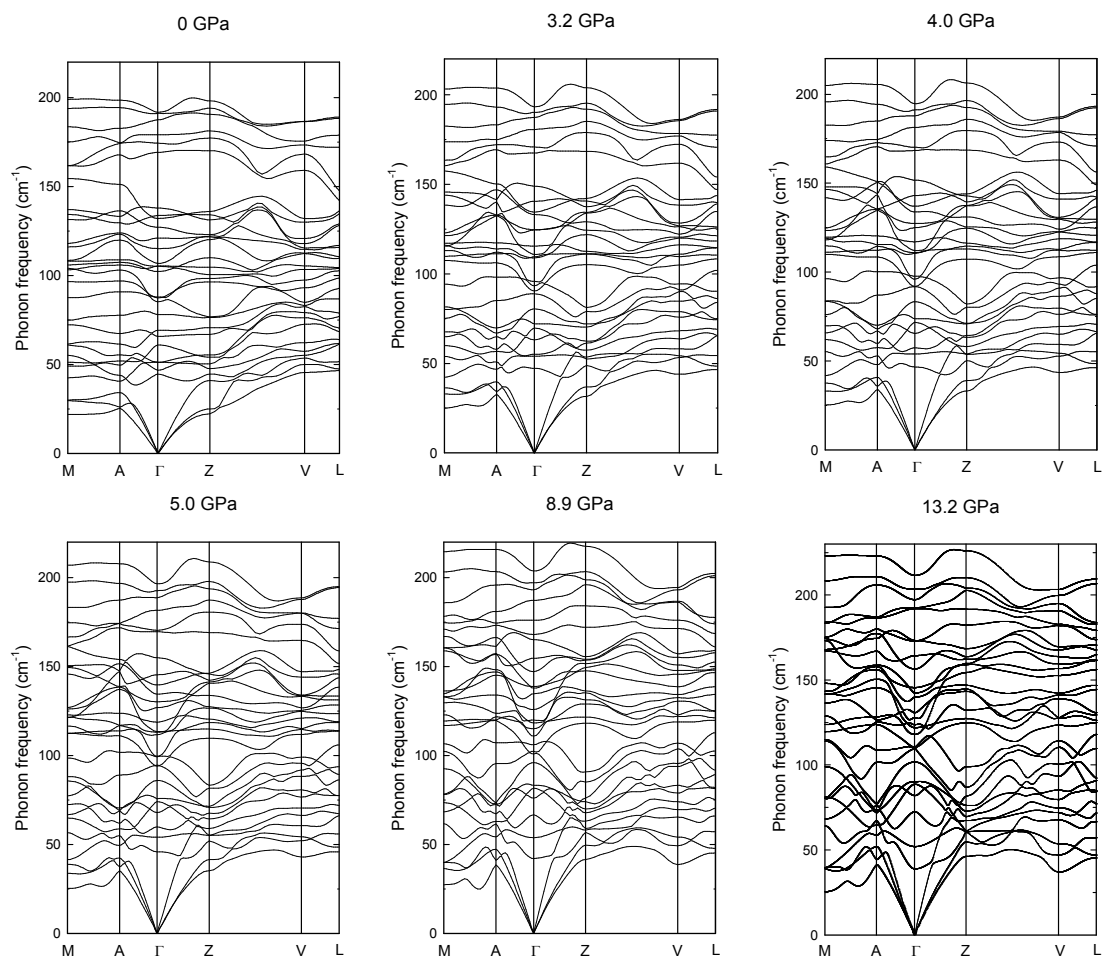


**Figure S16.** Theoretical phonon dispersion curves of  $\alpha\text{-As}_2\text{Te}_3$  at different pressures.

No soft phonon mode is observed either at  $\Gamma$  or at any other point of the Brillouin zone.

## References

- (1) Mendoza-Galván, A.; García-García, E.; Vorobiev, Y.V.; González-Hernández, J. Structural, Optical and Electrical Characterization of Amorphous  $\text{Se}_x\text{Te}_{1-x}$  Thin Film Alloys. *Microelectron. Eng.* **2000**, *51-52*, 677-687.
- (2) Usuki, T.; Saitoh, K.; Endo, M.; Uemura, O. Short-Range Order of Amorphous and Liquid As-Te-I System, *J. Non-Cryst. Solids* **1996**, *205-207*, 184-188.
- (3) Tverjanovich, A.; Rodionov, K.; Bychkov, E. Raman Spectroscopy of Glasses in the As-Te System. *J. Solid State Chem.* **2012**, *190*, 271-276.
- (4) Alekberov, R.I.; Mekhtiyeva, S.I.; Isayeva, G.A.; Isayev, A.I. Raman Scattering in As-Se-S and As-Se-Te Chalcogenide Vitreous Semiconductors, *Semic.* **2014**, *48*, 800-803.
- (5) Taylor, P.C.; Bishop, S.G.; Mitchell, D.L. Infrared Properties of  $\text{As}_x\text{Te}_{1-x}$  glasses, *Solid State Commun.* **1975**, *16*, 167-170.
- (6) Lukic, S.R.; Petrovic, D.M.; Skuban, S.J.; Radonjic, Lj.; Cvejic, Z. Formation of Complex Structural Units and Structure of As-S-Se-Te-I Glasses. *J. Opt. Adv. Mat.* **2003**, *5*, 1223-12229.
- (7) Zallen, R.; Slade, M.L.; Ward, A.T. Lattice Vibrations and Interlayer Interactions in Crystalline  $\text{As}_2\text{S}_3$  and  $\text{As}_2\text{Se}_3$ . *Phys. Rev. B* **1971**, *3*, 4257-4273.
- (8) Canepa P.; Hanson, R. M.; Ugliengo, P.; Alfredsson, M. J-ICE: a New Jmol Interface for Handling and Visualizing Crystallographic and Electronic Properties. *J. Appl. Cryst.* **2011**, *44*, 225-229.
- (9) Pereira, A. L. J.; Gomis, O.; Sans, J. A.; Pellicer-Porres, J.; Manjón, F. J.; Beltrán, A.; Rodríguez-Hernández, P.; Muñoz, A. Pressure Effects on the Vibrational Properties

of  $\alpha$ -Bi<sub>2</sub>O<sub>3</sub>: an Experimental and Theoretical Study. *J. Phys.: Condens. Matter* **2014**, *26*, 225401.

(10) Carron, G.J. The Crystal Structure and Powder Data for Arsenic Telluride. *Acta Cryst.* **1963**, *16*, 338-343.

(11) Haussühl, S. Physical Properties of Crystals. An Introduction, Wiley-VCH, Weinheim, 2007.

(12) Angel, R. J. [http://www.rossangel.com/text\\_strain.htm](http://www.rossangel.com/text_strain.htm)

(13) Zhao, J.G.; Yang, L.X.; Yu, Z.H.; Wang, Y.; Li, C.Y.; Yang, K.; Liu, Z.G.; Wang, Y. Structural Phase Transitions and Metallized Phenomena in Arsenic Telluride under High Pressure. *Inorg. Chem.* **2016**, *55*, 3907.

(14) Zhang, Y.H.; Ma, Y.M.; Geng, A.H.; Zhu, C.Y.; Liu, G.T.; Tao, Q.; Li, F.F.; Wang, Q.L.; Li, Y.; Wang, X. et al. Pressure-Induced Electronic Phase Transitions of  $\alpha$ -As<sub>2</sub>Te<sub>3</sub>. *J. Alloys Comp.* **2016**, *685*, 551-558.

(15) Deng, H. Theoretical Prediction of the Structural, Electronic, Mechanical and Thermodynamic Properties of the Binary  $\alpha$ -As<sub>2</sub>Te<sub>3</sub> and  $\beta$ -As<sub>2</sub>Te<sub>3</sub>. *J. Alloys and Comp.* **2015**, *656*, 695-701.

(16) Sakai, N.; Fritzsche, H. Semiconductor-Metal and Superconducting Transitions Induced by Pressure in Amorphous As<sub>2</sub>Te<sub>3</sub>. *Phys. Rev. B* **1977**, *15*, 973-978.

(17) Jacobsen, M.K.; Kumar, R.S.; Cornelius, A.L.; Sinogeiken, S.V.; Nicol, M.F. High Pressure X-Ray Diffraction Studies of Bi<sub>2-x</sub>Sb<sub>x</sub>Te<sub>3</sub> (x = 0,1,2). *AIP Conf. Proc.* **2007**, *955*, 171-174.

(18) Zhao, J.G.; Liu, H.Z.; Ehm, L.; Chen, Z. Q.; Sinogeikin, S.; Zhao, Y.S.; Gu, G. Pressure-Induced Disordered Substitution Alloy in  $\text{Sb}_2\text{Te}_3$ . *Inorg. Chem.* **2011**, *50*, 11291-11293.

(19) Souza, S.M.; Poffo, C.M.; Triches, D.M.; de Lima, J.C.; Grandi, T.A.; Polian, A.; Gauthier, M. High Pressure Monoclinic Phases of  $\text{Sb}_2\text{Te}_3$ . *Physica B* **2012**, *407*, 3781-3789.

(20) Ma, Y.M.; Liu, G.T.; Zhu, P.W.; Wang, H.; Wang, X.; Cui, Q.L.; Liu, J.; Ma, Y.M. Determinations of the High-Pressure Crystal Structures of  $\text{Sb}_2\text{Te}_3$ . *J. Phys.: Condens. Matter* **2012**, *24*, 475403.

(21) Gomis, O.; Vilaplana, R.; Manjón, F.J.; Rodríguez-Hernández, P.; Pérez-González, E.; Muñoz, A.; Drasar, C.; Kucek, V. Lattice Dynamics of  $\text{Sb}_2\text{Te}_3$  at High Pressures. *Phys. Rev. B* **2011**, *84*, 174305.

(22) Zhang, H.Y.; Cheng, Y.; Tang, M.; Chen, X.R. Ji, G.F. First-Principles Study of Structural, Elastic, Electronic and Thermodynamic Properties of Topological Insulator  $\text{Sb}_2\text{Te}_3$  under Pressure. *Comp. Mat. Sci.* **2015**, *96*, 342-347.

(23) Nakayama, A.; Einaga, M.; Tanabe, Y.; Nakano, S.; Ishikawa, F.; Yamada, Y. Structural Phase Transition in  $\text{Bi}_2\text{Te}_3$  under High Pressure. *High Pressure Res.* **2009**, *29*, 245-249.

(24) Polian, A.; Gauthier, M.; Souza, S.M.; Triches, D.M.; Cardoso de Lima, J.; Grandi, T. A. Two-Dimensional Pressure-Induced Electronic Topological Transition in  $\text{Bi}_2\text{Te}_3$ . *Phys. Rev. B* **2011**, *83*, 113106.

(25) Zhu, L.; Wang, H.; Wang, Y.; Lv, J.; Ma, Y.; Cui, Q.; Ma, Y.; Zou, G. Substitutional Alloy of Bi and Te at High Pressure. *Phys. Rev. Lett.* **2011**, *106*, 145501.

(26) Einaga, M.; Ohmura, A.; Nakayama, A.; Ishikawa, F.; Yamada, Y.; Nakano, S. Pressure-Induced Phase Transition of Bi<sub>2</sub>Te<sub>3</sub> to a bcc Structure. *Phys. Rev. B* **2011**, *83*, 092102.

(27) Vilaplana, R.; Gomis, O.; Manjón, F. J.; Segura, A.; Perez-González, E.; Rodríguez-Hernández, P.; Muñoz, A.; González, J.; Marín-Borras, V.; Muñoz-Sanjosé, V. et al. High-Pressure Vibrational and Optical Study of Bi<sub>2</sub>Te<sub>3</sub>. *Phys. Rev. B* **2011**, *84*, 104112.

(28) Ibarra-Hernández, W.; Verstraete, M. J.; Raty, J.-Y. Effect of Hydrostatic Pressure on the Thermoelectric Properties of Bi<sub>2</sub>Te<sub>3</sub>. *Phys. Rev. B* **2014**, *90*, 245204.

(29) Feng, S.; Li, S.M.; Fu, H.Z. First-Principle Calculation and Quasi-Harmonic Debye Model Prediction for Elastic and Thermodynamic Properties of Bi<sub>2</sub>Te<sub>3</sub>. *Comp. Mat. Sci.* **2014**, *82*, 45-49.

(30) Efthimiopoulos, I.; Zhang, J.M.; Kucway, M.; Park, C.; Ewing, R.C.; Wang, Y. Sb<sub>2</sub>Se<sub>3</sub> under Pressure. *Sci. Rep.* **2013**, *3*, 2665.

(31) Walsh, A.; Payne, D.J.; Egdell, R.G.; Watson, G.W. Stereochemistry of Post-Transition Metal Oxides: Revision of the Classical Lone Pair Model. *Chem. Soc. Rev.* **2011**, *40*, 4455-4463.

(32) Deringer, V.L.; Stoffel, R.P.; Wuttig, M.; Dronskowski, R. Vibrational Properties and Bonding Nature of Sb<sub>2</sub>Se<sub>3</sub> and their Implications for Chalcogenide Materials. *Chem. Sci.* **2015**, *6*, 5255-5262.